Journal of Power Sources 484 (2021) 229143

Contents lists available at ScienceDirect

Journal of Power Sources

journal homepage: www.elsevier.com/locate/jpowsour

Flexible quasi-solid-state lithium-ion capacitors employing amorphous SiO_2 nanospheres encapsulated in nitrogen-doped carbon shell as a high energy anode

Ranjith Thangavel [a,b,c], Vignesh Ahilan [d], Megala Moorthy [a], Won-Sub Yoon [b], Sangaraju Shanmugam [d,**], Yun-Sung Lee [a,*]

[a] Chonnam National University, Gwang-ju, 500-757, Republic of Korea
[b] Department of Energy Science, Sungkyunkwan University, Suwon, 440-746, Republic of Korea
[c] The Institute of New Paradigm of Energy Science Convergence, Sungkyunkwan University, Suwon, 440-746, Republic of Korea
[d] Department of Energy Science & Engineering, Daegu Gyeongbuk Institute of Science and Technology (DGIST), Daegu, 42988, Republic of Korea

HIGHLIGHTS

- Highly interconnected 3D SiO_2 nanospheres embedded Nitrogen-doped carbon shell.
- SiO_2 exhibits pseudocapacitive effect to enable a fast charge storage process.
- The Li-ion capacitor delivers high energy (139 Wh kg^{-1}) and power (42 kW kg^{-1}).
- Flexible Li-ion capacitor has stability at different bending conditions.

GRAPHICAL ABSTRACT

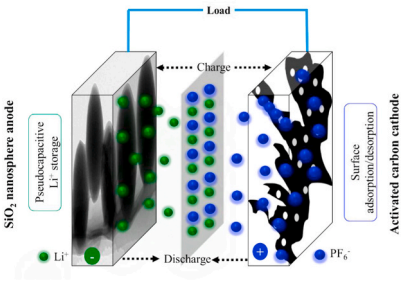

ARTICLE INFO

Keywords:
High capacity anode
Lithium-ion capacitor
SiO_2
Core-shell
Flexible device

ABSTRACT

Lithium-ion hybrid capacitors (LICs) take the advantage of simultaneous high energy – power output, and become increasingly important for next generation applications. Developing a high performing LICs with high energy-power-cycle combination remains a significant challenge due to low capacity intercalation electrodes, and kinetically sluggish alloying type electrodes. A strategy employing fast pseudocapacitive lithium ion storage in high-capacity alloying type anode, rather than a bulk storage, can output kinetically superior LICs with high energy even at high power conditions. Herein, we demonstrate a highly interconnected 3-dimensional (3D) SiO_2 nanospheres embedded Nitrogen-doped carbon shell with fast lithium ion storage kinetics as high performing anode for LICs. As a result, LIC with a high energy (139 Wh kg^{-1}), high power density (42 kW kg^{-1}), and super stability (20,000 cycles) is obtained, outperforming previously studied alloying type metal oxide and sulfide anodes. A flexible LICs is further demonstrated which shows good stability under different bending conditions. The current research promotes the practical utilization of earth-abundant material as a high capacity and high rate electrode for the next-generation flexible and wearable devices.

* Corresponding author.
** Corresponding author.
E-mail addresses: sangarajus@dgist.ac.kr (S. Shanmugam), leeys@chonnam.ac.kr (Y.-S. Lee).

https://doi.org/10.1016/j.jpowsour.2020.229143
Received 1 June 2020; Received in revised form 13 October 2020; Accepted 26 October 2020
Available online 23 November 2020
0378-7753/

1. Introduction

Lithium-ion based technologies are the most prominent device to serve portable electronic devices and have attracted tremendous attention towards next generation large-scale applications [1,2]. The research on next-generation storage device with simultaneous high energy and high power has seen an extensive growth during the past years to meet the demand for electric vehicle and hybrid electric vehicles applications [3,4]. The state-of-the-art lithium-ion batteries (LIBs) are severely limited by their low power density, and failure at high current densities due to sluggish intercalation storage kinetics. Although supercapacitors can deliver a high power, the energy output of supercapacitors cannot meet the demand. To address this issue, and to satisfy the emerging demands, a hybrid device merging the advantages of LIBs and supercapacitors – Lithium-ion hybrid capacitor (LIC) was proposed [5,6]. LICs use a battery type anode, and a capacitor type porous carbon cathode to combine the advantages of simultaneous faradaic Li-ion de/intercalation, and non-faradic surface reaction to achieve a high energy and high power [7,8].

The utilization of high capacity anode with superior rate capability with suitable working voltage is very essential to achieve a high performing LICs [9,10]. LICs have been previously studied with graphite based intercalation type anode, and several porous carbon based cathode [5,6]. However, the low capacity graphite anode limits the realization of high energy LICs [11,12]. Furthermore, the low lithium-ion intercalation potential (~0.2 V vs. Li) in graphite anode arises safety issues due to lithium dendrite growth. A high polarization at high current rates enhances the circumstances towards lithium dendrite formation, leading to safety issues in LICs [13].

Recently, Ti-based anodes have been investigated as an alternate, and significant progress in performance had been achieved. However, the low capacity and high intercalation potential negate the realization of high energy batteries [14,15]. More recently, V-based intercalation anodes are also studied as an alternative to commercial graphite. However, the fast active material deterioration impedes the long-term stability of LICs [16,17]. High capacity anodes working efficiently at high power with high stability are the key to the development of next-generation high energy LICs.

A variety of metal oxides and metal sulfides based on Sn, Cu, Ni, Mn, and Co utilizing alloying/conversion type Li-ion storage have been investigated for both LIBs and LICs [18–20]. However, they failed to achieve a high energy output due to sluggish Li-ion storage kinetics during conversion reactions [21,22]. Overcoming the sluggish reaction with fast pseudocapacitive Li-ion storage can be an eminent approach to simultaneously elevate the energy and power output. Recently, silica (SiO_2) has been proposed as a promising anode for LIBs because of their large lithium storage capacity, and a low voltage potential [23,24]. As the abundant element in earth's crust, SiO_2 could favorably develop a cheap next generation Li-ion storage device, and could be competing against other metal oxides. Nevertheless, SiO_2 suffers from intrinsic poor electrical conductivity and high volume expansion with repeated lithium insertion/extraction leading to poor rate performance and severe capacity fading.

Designing a nanostructured architecture such as nanotubes, nanowires, and nanosphere could overcome storage kinetics and volume expansion issues with repeated cycling [25,26]. While embedding the active SiO_2 nanoparticles into highly conductive carbon matrix could enhance the electrical conductivity of SiO_2 particles and thereby achieving a high rate capability [27,28]. Reddy et al. introduced nitrogen heteroatoms into the single dimensional graphene lattice, and achieved twice the capacity of the undoped graphene anode [29]. Nitrogen heteroatoms can enhance both the surface polarity, and the electrical conductivity, thereby improving the Li storage capability [30]. In synergy, 3D nanostructured SiO_2 constrained inside carbon shell can easily overcome by constraints, and volume changes on continuous lithium-ion insertion. Such nanoarchitecture can favor a significant pseudocapacitive effect to enable a fast charge storage process [31]. Utilizing the fast pseudocapacitive Li-ion storage anodes in LICs are highly promising to retain a high energy density even at high power conditions [32–34].

In this work, we synthesize and utilize nitrogen heavily doped and highly interconnected SiO_2 nanosphere inside the carbon nanoshell (SiO_2/NC) as a high performing pseudocapacitive anode for LICs. When employed in Li-ion half-cell, SiO_2/NC delivered a superior performance with a high discharge capacity of 858 mAh g^{-1} (0.1 A g^{-1}). Even at a higher current density of 5 A g^{-1}, SiO_2/NC delivered an adequate, capacity of ~275 mAh g^{-1} along with excellent capacity recovery. The SiO_2/NC can function efficiently even after 1000 cycles with a capacity of 480 mAh g^{-1} (1 A g^{-1}). When a LIC is constructed by coupling with commercial activated cathode, a high energy density of ~139 Wh kg^{-1} is realized, bridging the gap between low power batteries and low energy supercapacitors. The approach of utilizing alloying type anodes with pseudocapacitive Li-ion storage synergistically elevates the energy and power, outperforming conventional intercalation electrodes. The obtained performance was highly comparable to that of several previously reported metal oxides and sulfides based anodes [35,36]. The high performance is attributed majorly due to the 3D core-shell structured of SiO_2/NC embedded in highly conducting carbon network, resulted in fast lithium storage kinetics. Furthermore, an ultra-high stability for 20, 000 cycles with ~80% energy retention is noted.

In addition, the liquid electrolytes in LICs could pose a serious safety issues due to their highly flammable nature. Therefore, a safer device utilizing solid electrolytes, or quasi-solid state electrolytes must be realized. Realizing such devices can further attract flexible and wearable energy storage devices market [37]. Employing a Li-ion conducting P(VDF)-HFP polymer electrolyte matrix can integrate safety to the high energy LIC device. The assembled quasi-solid state LICs showed high flexibility, a good energy retention, and stability under different bending conditions. The realization of flexible LIC devices can shed light on development of highly safe, and high energy devices for next-generation applications.

2. Results and discussion

The synthesis process for core-shell SiO_2/NC nanosphere is shown in Scheme 1.The powder diffraction pattern in Fig. S1a shows a broad peak at 22°, revealing the amorphous nature of silica and carbon in SiO_2/NC sample, whereas another probable reason is that carbon peak overlaps with diffraction peak of SiO_2 nanosphere. A small shift of 24° (2Θ) peak for NC sample represents the presence of turbostratic nitrogen doped-carbon derived from the guanine source in NC sample. There is no observation of sharp peak for silica, which shows that SiO_2 was not reduced to Si, while on the hydrothermal reaction or at high-temperature calcination. The transformation from white color to black color powder is noted after formation heteroatom-doped carbon shell on the surface of SiO_2 nanosphere. The Raman spectrum of SiO_2/NC in Fig. S1b shows the presence of G and D-bands which are characteristic of peaks of carbon originating from graphitic sp^2 carbon atom planes, and defect-induced vibration from carbon planes, respectively [38,39]. The N_2 adsorption/desorption isotherm of SiO_2/NC (Fig. S1c) shows Type-IV behavior, indicating the presence of large number of mesopores that facilitate easy ion/electron pathway. The BET surface area of the SiO_2/NC material is 35 m^2/g, and no significant remark on micropores is noted from adsorption isotherm.

The SEM morphology studies show the nanosphere morphology of SiO_2 particles, and well connected with nitrogen-doped carbon shell. The average diameter of SiO_2 nanospheres is ~200 nm (Fig. 1a and Fig. S2). The TEM images in Fig. 1b confirms the highly interconnected, smooth. and uniform spherical nature SiO_2/NC. The HRTEM image in Fig. 1c further confirms the presence of a thin layer of nitrogen-doped carbon nanoshell on the surface of SiO_2 core. The EDX elemental mapping image of SiO_2/NC (Fig. 1d–h) shows the uniform distribution of

carbon and nitrogen heteroatoms over the on the surface of SiO_2 nanospheres. The presence of nitrogen heteroatoms in the body of SiO_2 indicates the possibility of presence of nitrogen doping in oxygen atoms of SiO_2 [40]. The SiO_2/NC spheres are continuously connected, and this morphology enable a continuous electron and lithium ion movement [41,42]. Generally, a rigid carbon coating tends to crack upon cycling, and the coulombic efficiency drops rapidly after few cycles, and thereby degrading the performance of LIBs. However, a thin carbon layer can facilitate uniform electrode-electrolyte interface layer, and deliver a stable coulombic efficient upon cycling [9,38].

TGA data are shown in Fig. S3 confirms that the amount of carbon content in SiO_2/NC. There are two steps of weight loss, starting from 40 °C to 500 °C, mainly due to the removal of organic compounds like hydroxyl group and oxygen group presence in the surface of the material [43]. The second weight loss begins at 500 °C continues till 800 °C, it obviously from the oxidation of carbon in the material [44]. These results significantly show that 24.8 wt % of carbon content in SiO_2/NC. Elemental (C, H, N, S) analysis is further utilized to confirm the amount of carbon in SiO_2/NC sample. The amount of carbon in SiO_2/NC is evaluated to be ~21.4 wt%, and additionally, the amount of nitrogen is calculated to be ~4.2 wt% in SiO_2/NC, which is a close value obtained from the TGA results. The XPS survey spectrum (Fig. 1i) of SiO_2/NC confirms the presence of Si, O, N and C elements [45,46]. The deconvoluted Si2p spectrum (Fig. 1j) of SiO_2/NC shows the peaks centered at 103.5 eV attributed to tetravalent state of Si in SiO_2. To understand the chemical nature of nitrogen, N1s spectra (Fig. 1k) is deconvoluted, and it shows the presence of pyridinic (398 eV) and pyrrolytic (401 eV) type of nitrogen species [47–50]. The content of nitrogen doping, especially that of the presence of pyrolytic nitrogen, in SiO_2/NC material would show higher and is believed to benefit the electrical conductivity and provide additional anchoring sites for Li-ions, giving rise to higher lithium storage capacity [51].

2.1. Half-cell performance

The lithium storage mechanism in SiO_2/NC is majorly by the alloying/de-alloying reaction. Cyclic voltammetry was used to investigate the lithium storage process of the SiO_2/NC anode, and Fig. 2a shows the CV curves of SiO_2/NC between 3 and 0.01 V at 0.1 mV s^{-1}. The first cathodic discharge scan shows two broad irreversible reduction peak at ~1.3 V and ~0.65 V, attributed to electrolyte decomposition and formation of solid electrolyte interface (SEI) layer over the particle surface which is very common for lithium anodes [52]. From the consecutive cycles, CV curves show a redox peak around ~0.65 V during the cathodic scan and ~1.1 V during the anodic scan. The shape of the CV curves is well preserved, indicating reversible lithium storage in SiO_2 anode. The lithium storage behavior in SiO_2 is not known and still under debate, and different storage mechanisms have been proposed by several research groups [25–28]. The lithium storage begins with the formation of an irreversible Li_2O and lithium silicate ($Li_2Si_2O_5$) phase, consuming a large irreversible capacity during first discharge, along with formation of metallic silica (Si). The metallic silica further undergoes alloying/conversion type lithium storage that are highly reversible on consecutive cycles. The Li-ion storage mechanism in amorphous SiO_2 based anode materials during discharging and charging process are shown in equations (1) to (5) [53,54].

Discharge reaction:

$$SiO_2 + (4/5)Li^+ + (4/5)e^- \rightarrow (2/5)Li_2Si_2O_5 + (1/5)Si \ldots. \quad (1)$$

$$SiO_2 + 2Li^+ + 2e^- \rightarrow (1/2)Li_4SiO_4 + (1/2)Si \ldots \ldots \ldots \ldots \ldots \quad (2)$$

$$Si + (15/4)Li^+ + (15/4)e^- \rightarrow (1/4)Li_{15}Si_4 \ldots \ldots \ldots \ldots \ldots \ldots \quad (3)$$

Charge reaction:

$$Li_{15}Si_4 \rightarrow 15Li^+ + 4Si + 15e^- \ldots \ldots \ldots \ldots \ldots \ldots \ldots \ldots \ldots \ldots \quad (4)$$

$$Li_2Si_2O_5 + (1/2)Si \rightarrow (5/2)SiO_2 + 2Li^+ + 2e^- \ldots \ldots \ldots \quad (5)$$

The charge-discharge voltage profiles of SiO_2/NC at 0.1 A g^{-1} is shown in Fig. 2b. The first discharge curves show an irreversible plateau ~0.65 V corresponding to formation of SEI layer and irreversible Li_2O and lithium silicate ($Li_2Si_2O_5$) phase. The SiO_2 delivered a discharge capacity of ~2450 mAh g^{-1} at 0.1 A g^{-1}, among which 858 mAh g^{-1} was reversible during consecutive charging. Although a low initial coulombic efficiency (35%) was shown, stable and reversible lithium storage in consecutive cycles pushes the efficiency to near 99%. The SiO_2/NC exhibited a very low initial capacity loss and discharge capacity stabilized from 5th discharge with capacity ~840 mAh g^{-1} and maintained excellent lithium storage after that. Note that the capacity includes the combined mass of both SiO_2 nanospheres and nitrogen doped carbon shell. The capacity retention after the 150th cycle is 102% with discharge capacity ~858 mAh g^{-1}, depicting the possibility of huge and highly reversible lithium storage behavior with SiO_2/NC (Fig S4).

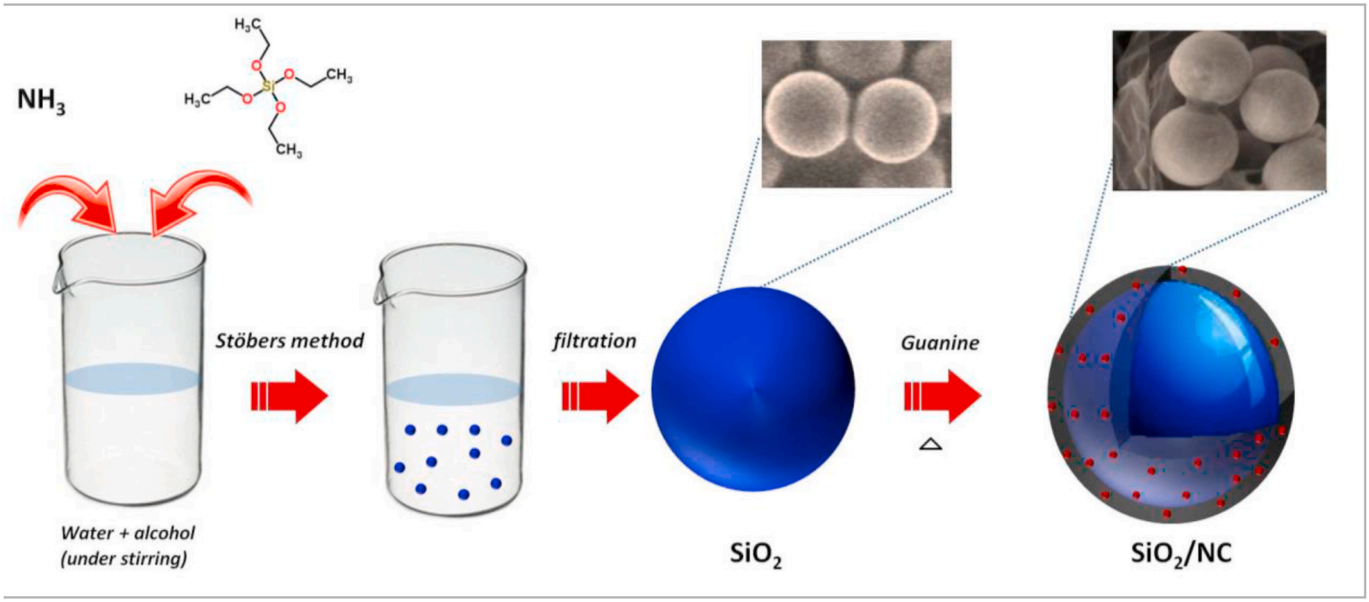

Scheme 1. Schematic representation of fabrication process for core-shell SiO_2/NC nanosphere.

High rate performance and robust cycling performance is crucial for lithium-ion storing anodes. The rate performance of SiO_2 and SiO_2/NC is performed at various currents and presented in Fig. 2c and d. A superb high rate capability has been demonstrated by SiO_2/NC, delivering a discharge capacity of ~780, 604, 438, and 337 mAh g^{-1} at 0.25, 0.5, 1, and 2 A g^{-1}, respectively. Even at an extremely high current of ~5 A g^{-1}, SiO_2/NC, efficiently stored lithium ions and delivered ~275 mAh g^{-1}. In contrast, pristine SiO_2 cannot withstand high current conditions and fails under such robust condition, delivering a poor discharge capacity of 330, and 40 mAh g^{-1} at 0.25 and 5 A g^{-1}, respectively. This result shows the failure of alloying/de-alloying reaction in pristine SiO_2 without carbon environment. Additionally, SiO_2/NC showed excellent capacity recovery ability by retaining the discharge capacity ~613 mAh g^{-1} when the current was brought back to 0.5 A g^{-1}. Such a superior performance is synergistically enhanced by high electronic conductivity in the carbon shell by nitrogen heteroatoms. The performance of SiO_2/NC is compared with other nanostrutred SiO_2 anodes in Table 1, and it can be observed that SiO_2/NC delivered a superior performance.To further evaluate the kinetic properties, EIS was measured for pristine SiO_2, and SiO_2/NC. The Nyquist plots of pristine SiO_2, SiO_2/NC (Fig. S5) clearly shows the charge transfer resistance for SiO_2/NC was very much reduced, compared to that of the pristine SiO_2. The introduction of carbon shell containing nitrogen hetero atoms greatly improves the kinetics of Li-ion. The nanosphere morphology can also provide a large number of active lithium storage reaction sites. The favorable design of placing the SiO_2 particles over carbon platform can provide fast lithium kinetics and electron flow between SiO_2 particles through the shorter path and thereby overcome any lithium diffusion limitations at higher current. In absence of carbon shell, the electronic flow between the SiO_2 particles becomes negligible, and thereby making incomplete alloying reactions. The highly dense, and spherical morphology of SiO_2 nanoparticles can increase the packing density, and is highly beneficial for achieving a high volumetric capacity. To evaluate the electrode-packing density of SiO_2/NC, the materials were pressed into a thin film under a high pressure 100 MPa, and the electrode-packing density of SiO_2/NC is calculated to be ~1.3 g/cc. The corresponding volumetric capacity of the SiO_2/NC can reach ~1014, 785, 569, 438, 357 mAh cc^{-1} at 0.25, 0.5, 1, 2, and 5 A g^{-1}, much higher than conventional graphite anode [55].

The cyclic voltammetry was performed to elucidate the high Li ion storage kinetics in SiO_2/NC, at different scan rates (0.2–3 mV s^{-1}), and it can be seen that the shape profile of CV curves are well maintained even at high scan rates, indicating a faster lithium storage kinetics (Fig. 3a). In general, the current response (i) at a particular voltage contains pseudocapacitive contribution ($k_1\nu$) and diffusion-limited contribution ($k_2\nu^{1/2}$) and is in exponential relationship with scan rate (ν).

$$i = k_1\nu + k_2\nu^{1/2} = a\nu^b$$

Here, k_1, k_2 and a are constants, b-value of 0.5 indicates a diffusion limited lithium storage while the b-value of 1 indicated pseudocapacitive lithium-ion storage. The scan rate and output current response in CV curves are directly proportional with the b-value of ~0.91 (Fig. 3b), indicating a surface limited pseudocapacitive lithium storage in SiO_2/NC. Such surface limited pseudocapacitive lithium storage can facilitate

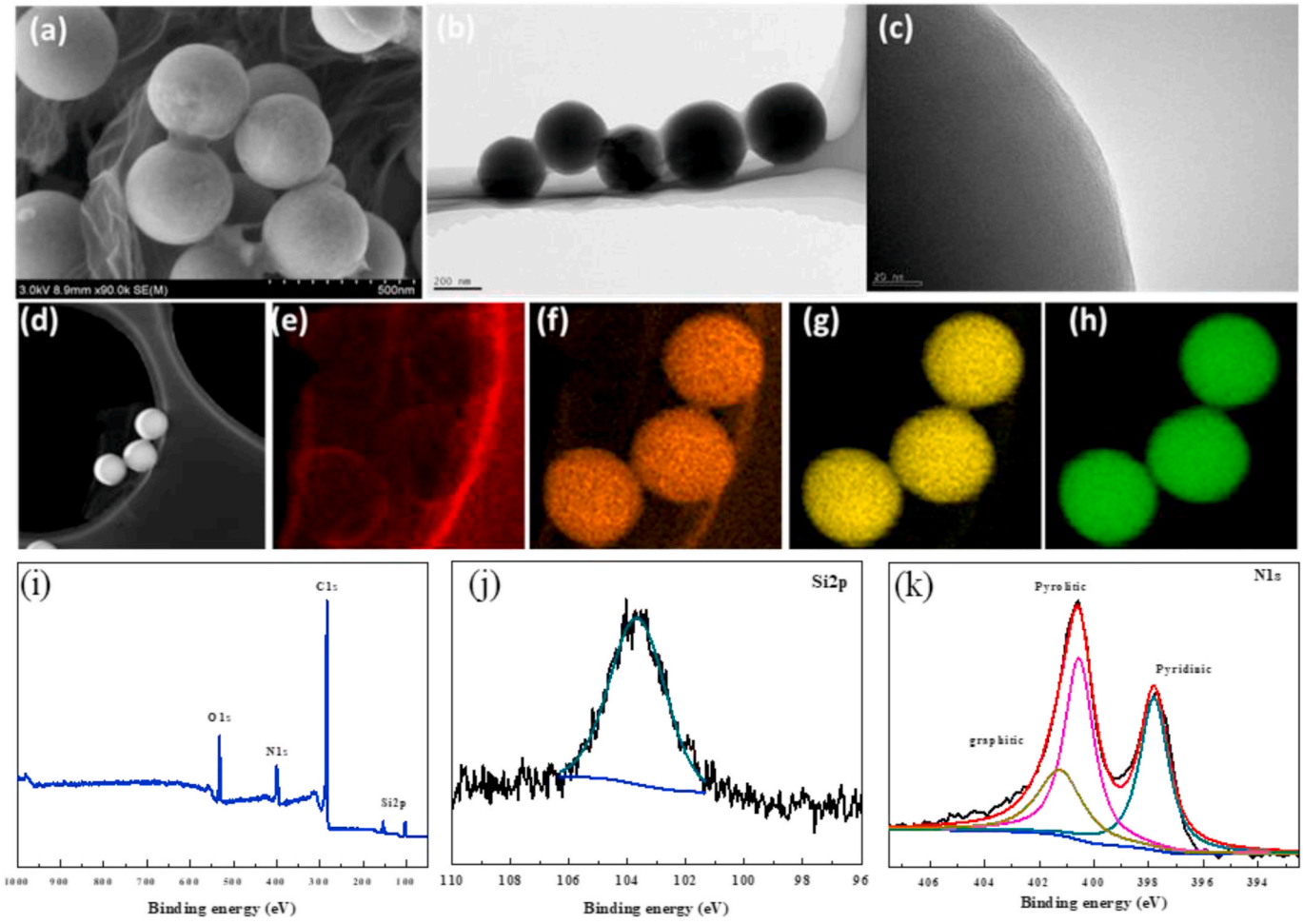

Fig. 1. (a) SEM image of SiO_2/NC, (b) TEM image of SiO_2/NC, (c) HRTEM image of SiO_2/NC, (d) Bright-field TEM image of SiO_2/NC and corresponding elemental mapping analysis for (e) Carbon (f) Nitrogen (g) Si and (h) Oxygen, (i) XPS spectrum of SiO_2/NC, and de-convoluted XPS spectrum of (j)Si2p, and (k) N1s.

ultra-fast lithium-ion storage than convention anodes with sluggish diffusion limited lithium storage. The high pseudocapacitive lithium-ion storage is ascribed to the short lithium ion diffusion length and rapid electron flow due to favorable 3D nanoarchitecture. The 3D spherical architecture provides a large electrode-electrolyte contact area and favors quick pseudocapacitive storage. By calculating the k_1, k_2 values at a different voltage (Fig. S6), the ratio of capacitive lithium storage is evaluated and given in Fig. 3c. Moreover, a high pseudocapacitive contribution of ~92% towards lithium-ion storage is observed at 1 mV s^{-1}.

The long-term cycling performance of SiO_2/NC was evaluated directly at 0.5 A g^{-1} without any prior activation at low current, and the results are shown in Fig. S7. A slight and quick capacity decay during initial cycles were noted, and the capacity gets stabilized with ~600 mA h g^{-1} within few cycles. After that SiO_2/NC showed robust stability in which capacity increases after specific cycles. This feature is more pronounced in alloy type anodes due to later activation of metal with cycling [56]. The non-metallic silica nanoparticles formed during the initial cycles are not activated earlier but get activated upon further cycling, and the capacity after the 500th cycle is 525 mAh g^{-1}. With extended cycling, SiO_2/NC can efficiently store lithium ion for 1000 cycles with ultra-low capacity degradation and the discharge capacity after the 1000th cycle is ~450 mAh g^{-1}. However pristine SiO_2 showed a continuous capacity degradation even under low current rate (Fig. S8). The long-term cyclability of SiO_2/NC was also studied at 1 A g^{-1} (Fig. 3d), and it demonstrated remarkable stability at higher current density also, along with high capacity retention even after 1000 cycles. For the practical LIBs, a superior stability at high areal mass loading is very essential, and so, SiO_2/NC is tested under a high areal mass loading of ~3.5 mg cm^{-2} at 0.5 A g^{-1} (Fig. 3e) [57]. Although a slight capacity reduction is noted under high mass loading condition SiO_2/NC exhibited a similar capacity retention as low loading conditions (2 mg cm^{-2}). The 3D architecture of SiO2/NC can overcome the kinetic issues, and pulverization issues as observed in conventional anodes. And, a robust stability in alloying type SiO_2 anode outperforms previous reports, where a substantial volume change affects the stability and electrochemical performance.

Table 1
A comparison on SiO_2 based anode materials for lithium-ion battery.

Anode Material	Current density	Initial charge-discharge specific capacity	Reversible capacity	Cycle number
SiO_2@C hollow spheres [71]	0.11 mAcm^{-2}	318.7/153.6	649.6	160
Carbon-coated silica macromolecules [72]	0.2 mAcm^{-2}	281/95	222	100
Carbon coated SiO_2 nanoparticles [73]	50 mAg^{-1}	536/900	500	50
SiO_2-Carbon [74]	70 mAg^{-1}	1055/458	601	100
SiO_2 –graphene composite [75]	500 mAg^{-1}	–	300	110
SiO_2 nanocubes [25]	100 mAg^{-1}	3084/1457	919	30
SiO_2/NC (our work)	100 mAg^{-1}	2450/858	858	**1000**

This high performance is achieved mainly by embedding the SiO_2 nanospheres between nitrogen-doped carbon outer-shell. Any volume changes can be easily accommodated by nanosphere regime between highly conductive carbon outer-shell. To validate the reason and to obtain insight, ex-situ TEM images of SiO_2/NC was taken after cycling and given in Fig. S9. The TEM images of SiO_2/NC after cycling shows the

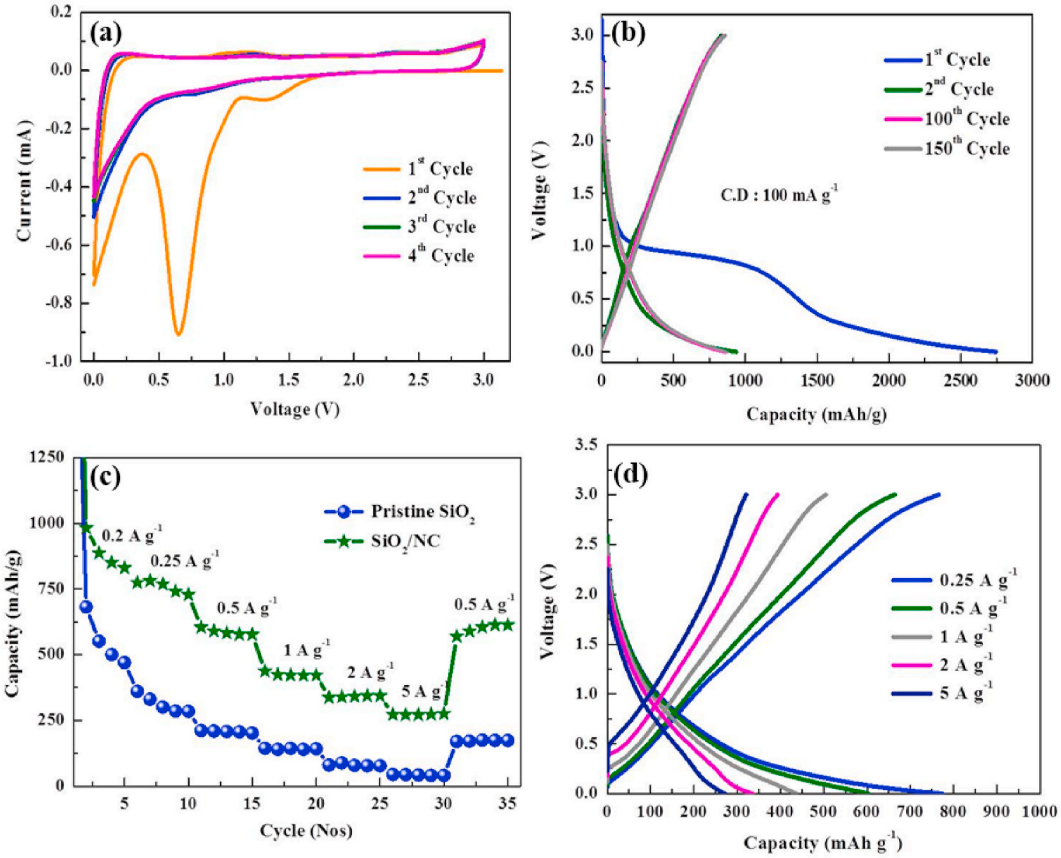

Fig. 2. (a) CV curves of SiO_2/NC at 0.1 mV s^{-1} vs. Li/Li^+, (b) Galvanostatic charge-discharge voltage profiles of SiO_2/NC at 100 mA g^{-1}, (c) Rate performance of SiO_2/NC comparison with pristine SiO_2, (d) galvanostatic charge-discharge voltage profiles of SiO_2/NC at different current rates.

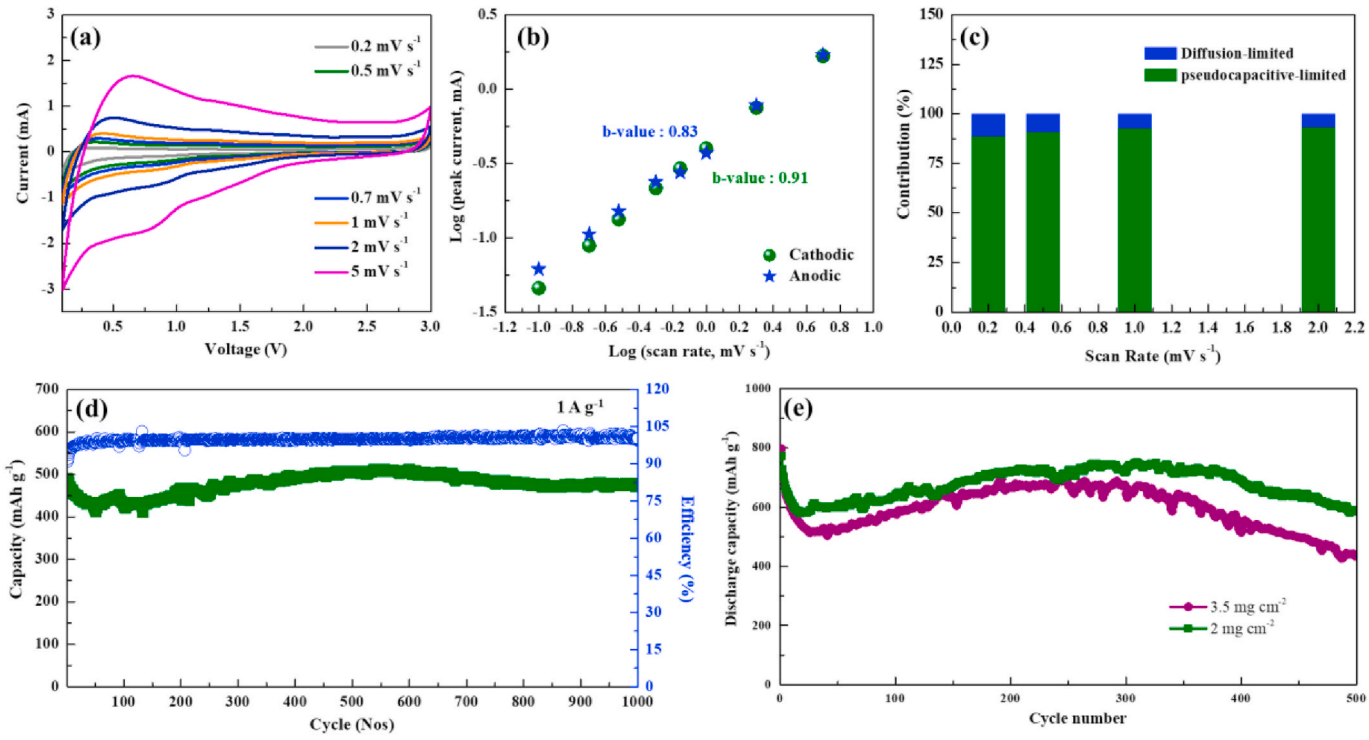

Fig. 3. (a) CV curves of SiO_2/NC at different scan rate, (b) current vs. scan rate relationship for SiO_2/NC, (c) charge storage contributions at different scan rates, (d) cyclic stability at 1 A g^{-1}, and (e) Cyclic stability under different mass loading conditions (0.5 A g^{-1}).

spherical morphology of SiO_2 particles is well preserved, and the carbon shell well adheres to particles even after robust cycling. Additionally, the nanospheres are well interconnected which is crucial for the continuous electron and lithium ion movement between the particles. The lithium ion and electron flow path are substantially diminished with nanostructure and thereby favors high rate performance. The perfect integrity of SiO_2/NC particles plays a crucial role in maintaining high stability even with repeated alloying – dealloying reactions.

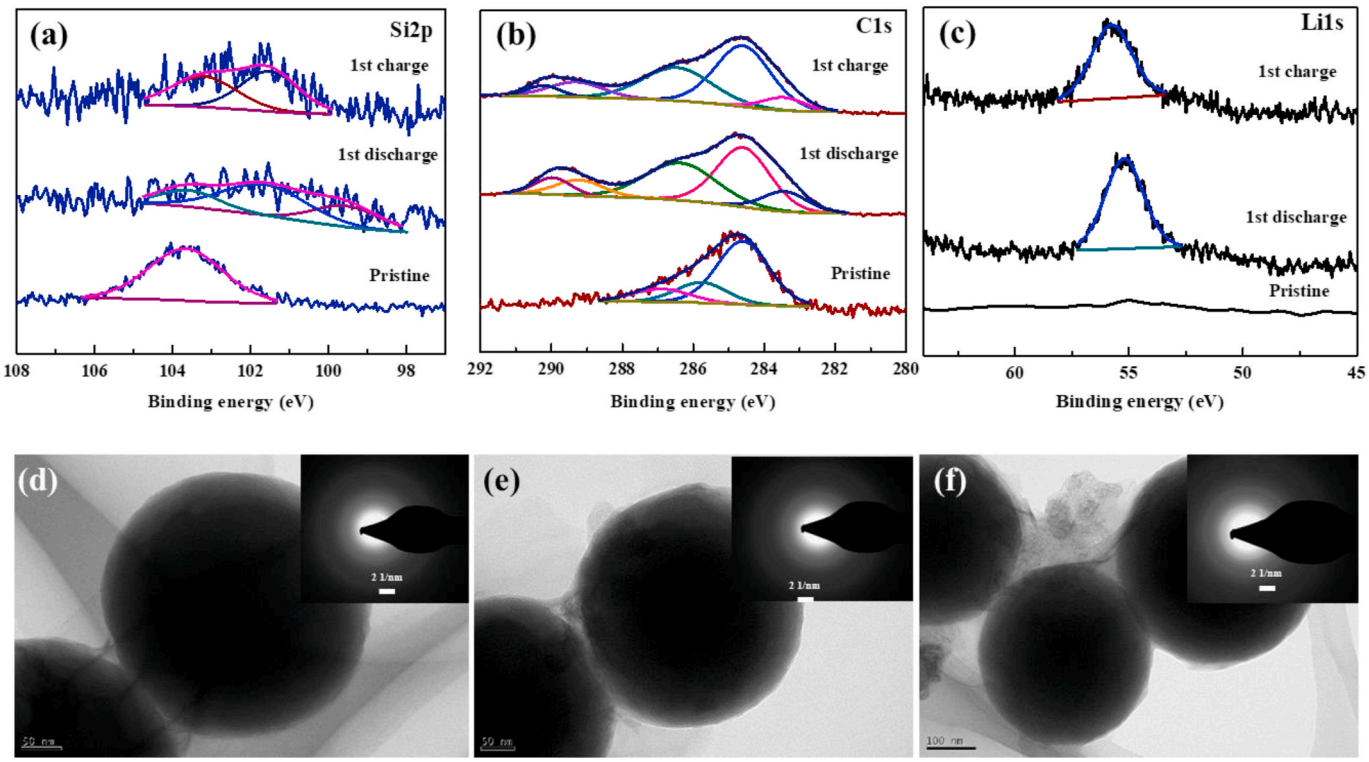

Fig. 4. Ex-situ XPS spectrum of SiO_2/NC recorded at different state (a) Si2p, (b) C1s, (c) Li1s, and Ex-situ TEM images of SiO_2/NC (d) before cycling, (e) after 1st discharge, (f) after 1st charge.

The lithium storage behavior in SiO_2/NC is further evaluated by ex-situ XPS technique obtained before cycling and at first discharge and charge state in Fig. 4. The Si 2p spectrum (Fig. 4a) of SiO_2/NC before cycling shows a strong SiO_2 peak at ~103.8 eV and after first discharge/charge process, a slight shift is observed in it, indicating the formation and decomposition of $Li_2Si_2O_5$. Moreover, a peak at ~101.5 eV, indicates the formation of Li_4SiO_4 and other Li_xSiO_y phases and these new peaks are still present even after delithiation, indicating the irreversibility of such phases. More importantly, the peak at ~99.6 eV indicates the formation of metallic silicon during discharge and disappears on a subsequent charge which is in correlation with previously discussed reaction mechanism [58–60]. Therefore, it is confirmed that there is the reversible reaction of $Li_2Si_2O_5$ and metallic Si and the irreversible reaction of Li_4SiO_4 phase. The formation of SEI layer is further analyzed by deconvoluted C1s spectrum in Fig. 4b. It can be seen the formation of –CO (290.2 eV), and *O*–C═O (289.2 eV) functionalities over C1s after first lithiation process and still available after delithiation process. This observation indicates the formation of the highly stable passivation layer over the SiO_2/NC particles. Furthermore, Li_{1S} spectrum (Fig. 4c) which is not present in SiO_2/NC before cycling is also present at ~55.2 eV indicating the formation of smooth SEI layer over SiO_2/NC. The TEM images of SiO_2/NC recorded after first lithiation and de-lithiation in Fig. 4d–f, and Fig. S10 shows that the spherical morphology of SiO_2/NC is well maintained without any volume expansion, indicating their structural integrity. Additionally, the SAED pattern obtained after first discharge still shows the amorphous nature indicating the discharge products such as $Li_2Si_2O_5$, Si, Li_4SiO_4, $Li_{15}Si_4$ are still amorphous and this nature is well maintained after consecutive charge cycle. Such type

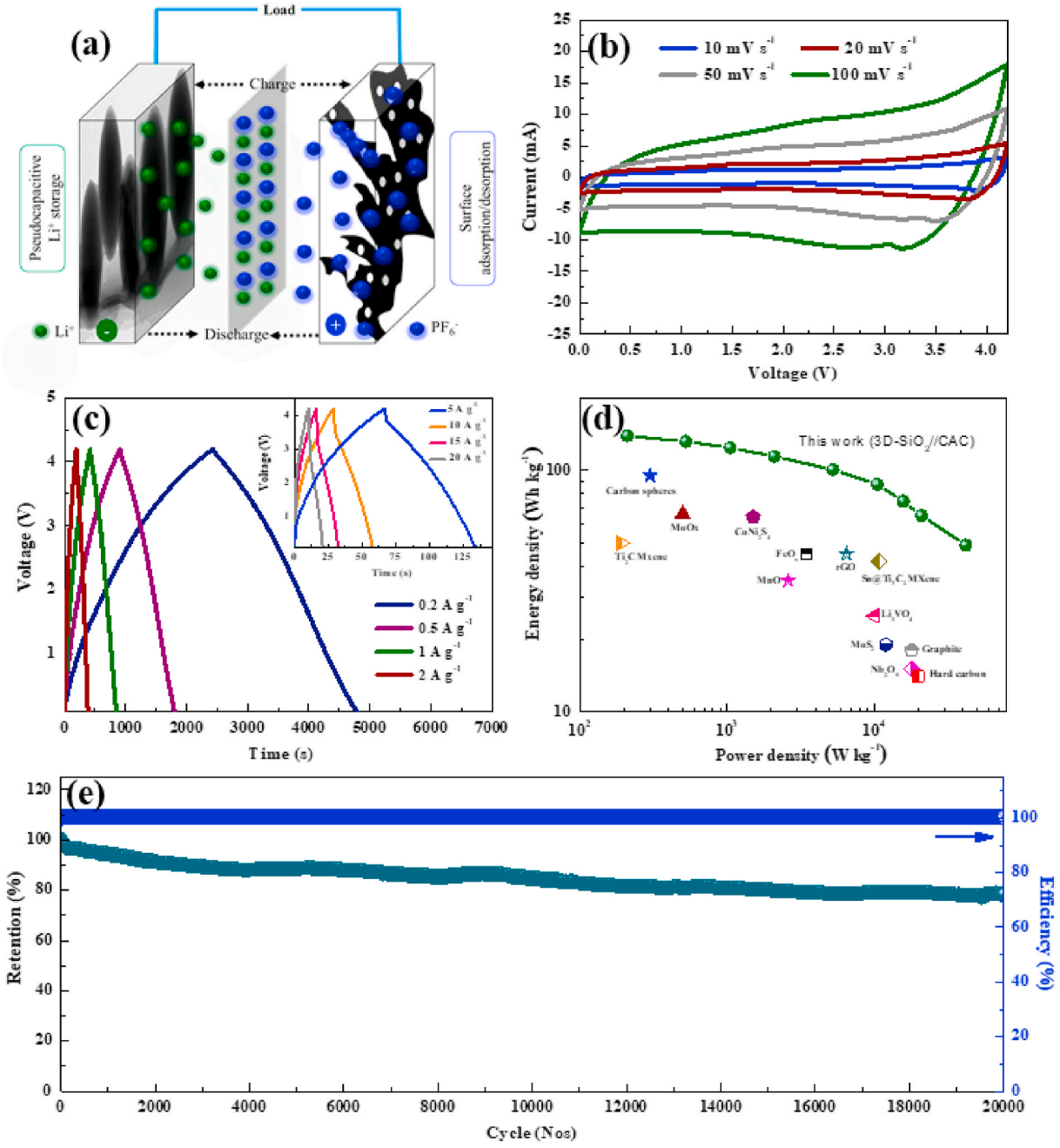

Fig. 5. Electrochemical Performance of LICs: (a) scheme on working mechanism, (b) CV curves, (c) CD curves at different current densities, (d) Ragone plot comparison with other systems, and (e) cyclic stability at 7.5 A g^{-1}.

of amorphous type of conversion and the alloying reaction is highly favorable for high capacity and stable lithium-ion storage.

To further understand the formation of SEI layer which is majorly Li_2CO_3 and alkyl carbonates over the SiO_2/NC surface, electrochemical impedance spectroscopy was performed after first discharge and first charge (Fig. S11a). The fresh SiO_2/NC electrode shows a single large semi-circle at high-frequency region and followed by a Warburg impedance tail at low-frequency region originating from Li-ion diffusion into SiO_2/NC. This was due to the rapid charge transfer at the electrode/electrolyte interface and enhanced reaction kinetics of the electrode material. After the first charge, the Nyquist plot shows two semi circles - the semi-circle in the high-frequency region is attributed to surface passivation SEI layer, and the other semi-circle at mid-frequency region corresponds to charge transfer resistance at electrode/electrolyte interface. On subsequent de-lithiation process, the two semi-circles changes to one indicate a partial decomposition of SEI layer due to significant volume expansion but with decreased charge transfer resistance. This could be attributed to the spherical architecture of SiO_2/NC anode that provides increased electrode/electrolyte contact area for lithium ion diffusion, and such phenomenon has been observed for other alloying type anodes [61,62] Even after cycling the change in charge transfer resistance is much smaller, indicating a superior lithium storage kinetics and stability in SiO_2/NC (Fig. S11b). The reduced charge transfer resistance is ascribed to enhanced lithium ion and electron movement in SiO_2 with nitrogen-doped carbon shell which facilitates the formation of the highly stable passivation layer over the SiO_2/NC particle [63].

2.2. Li-ion hybrid capacitor

Hybrid devices employ a capacitor type porous carbon cathode as adsorption electrodes for anions. Activated carbons (ACs) are traditionally used as cathode for LICs because of their high surface area. A hybrid device is fabricated by coupling SiO_2/NC as anode and ACs as cathode (Fig. 5a) and the electrochemical performance of LIC is evaluated between a wide voltage window (0–4.2 V). The CV curves of SiO_2/NC//AC hybrid device shows a quasi-rectangular shape profile with humps and it is well observed at all scan rates (Fig. 5b). Even at very high scan rate of 100 mV s^{-1}, the CV curves are well retained indicating the fast kinetics of LIC device. The current response from the CV curves are also noted to be linear with scan rate confirming the fast pseudocapacitive type reaction in LICs [64].

The charge-discharge curves of LICs in Fig. 5c shows a symmetric and nearly linear behavior with high coulombic efficiency, confirming the reversible nature of faradaic pseudocapacitive reactions in LICs. The reaction mechanism in LIC is as follows: (i) during charge process, anions (PF_6^-) are adsorbed over porous carbon cathode, while Li-ion from electrolyte gets stored in SiO_2/NC anode, and (ii) during discharge process, reversal of charge process occurs. Even at high current rates (20 A g^{-1}), a high discharge time is observed, indicating the superior rate capability and kinetics of the LIC device.

The energy-power performance of LIC is evaluated by Ragone plot in Fig. 5d. The LIC constructed with SiO_2/NC delivered a high energy of ~139 Wh kg^{-1} at a power density of 210 W kg^{-1}. Even at an ultra-power energy density of 42,000 W kg^{-1}, a high energy density of 52.5 Wh kg^{-1} is retained. The energy density behavior is far higher than the conventional electrical double layer capacitors (EDLCs) which often shows energy density less than 30 Wh kg^{-1}. It is also very essential to compare the energy – power behavior of the SiO_2/NC device with previously reported LICs and is show in Fig. 5d and Table S1. The Ragone plot clearly depicts the superior performance of the SiO_2/NC system with high energy along with high power. In particular, the energy retention at high power conditions are remarkable with superior to several previously reported LIC and sodium-ion hybrid capacitors system based on intercalation compounds (TiO_2, $Li_4Ti_5O_{12}$, V_2O_5), alloying type - metal oxides (Fe_3O_4, Nb_2O_5, WO_3, MnO), metal sulfides (CoS_2, SnS_2), metals (Si, Sn), bi-metallic compounds (Mxenes, $CoNi_2S_4$ Co_3ZnC) and nanostructured carbon [5,12,64–67]. In addition, the LICs employing SiO_2 delivered a remarkable stability, outperforming several previously reported anodes. Moreover, the LIC exhibited a remarkable stability with ~80% capacitance along with high coulombic efficiency even after 20,000 cycles when tested at current density of 7.5 A g^{-1} (Fig. 5e). The stability outperforms the low cycle behavior exhibited by alloying type anodes. A flexible LIC is constructed by coupling SiO_2/NC anode, commercial AC cathode, and Li-ion conducting gel polymer electrolyte P(VDF-HFP) membrane. The polymer membrane possess a lot of pores that efficiently allows ion movement while providing high flexibility to the electrodes [38,68]. Fig. 6a shows the normalized energy density of as-fabricated flexible LICs, and it can be noted that the LICs output a steady energy output at different bending conditions. The as fabricated flexible LIC can steadily light “Red and White LEDs”, and the flexible LICs can steadily light LEDs even under different bending/twisted conditions, indicating the robustness of the flexible LICs (Fig. 6b–f). The flexible LIC can also retain high energy even under bending conditions, depicting the high safety of the device. The synergistic effect from high capacity SiO_2 anode, and Li-ion conducting P(VDF-HFP) gel electrolyte outputs a flexible LIC with superior bendability.

The attractive performance of lithium-ion hybrid capacitor is majorly attributed to following factors. The well-connected - carbon shell supported SiO_2 nanospheres bridges inherits the advantage of the high active surface area for fast Li-ion diffusion and electron flow. Most importantly such nanostructures significantly enhance the charge transfer resistance by providing short lithium and electron transport path. This architecture is highly favorable for achieving a large amount of lithium ion storage and so the LICs have high energy density even at high power conditions. This is synergistically supported by nitrogen heteroatoms over the carbon shell. The fast pseudocapacitive lithium-ion storage overcomes the sluggish diffusion limited storage to enable a fast lithium-ion storage and thereby achieving a high power density. A highly stable lithium-ion storage behavior is achieved by design strategy of embedding the SiO_2 nanosphere into highly conductive heteroatom doped carbon shell. This design dramatically enhances the structural integrity of active material by overcoming the large the volume changes during repeated alloying and de-alloying reactions.

3. Conclusion

We have demonstrated SiO_2 nanospheres embedded inside nitrogen-doped carbon shell as high performing pseudocapacitive anode materials for LIBs and LICs. The SiO_2/NC exhibited lithium storage with high discharge capacities of 858 mAh g^{-1} at 0.1 A g^{-1}, 275 mAh g^{-1} at 5 A g^{-1}, and 450 mAh g^{-1} after 1000 cycles in half-cell configuration, which is the best performance documented by SiO_2 anodes. In a Li-ion hybrid capacitor full-cell, SiO_2/NC outputs a high energy (139 Wh kg^{-1}), and high power density (42 kW kg^{-1}) – based on active mass in both electrodes, along with prolonged stability (20,000 cycles – 80%). The attractive electrochemical performance is competitive against conventionally studied metal oxide/sulfide anodes and encourages the research with an earth abundant material. The 3D architecture SiO_2 in highly conductive carbon network favors a large and fast lithium ion uptake. The well interconnected SiO_2 nanospheres confined in carbon shows high mechanical bonding that demonstrated excellent stability and rate performance. We believe the 3D nanoarchitecture design utilizing the earth abundant anode material hold great promise in next generation high energy and low-cost storage systems.

4. Experimental section

Synthesis of SiO_2 nanosphere: The SiO_2 nanospheres were synthesis based on renowned Stöber method [69,70]. A mixture of absolute ethanol, ammonia and distilled water in the volume ratio of 158:7.8:2.8 in a 250 mL round bottom flask at a 50 °C, under stirring, followed by

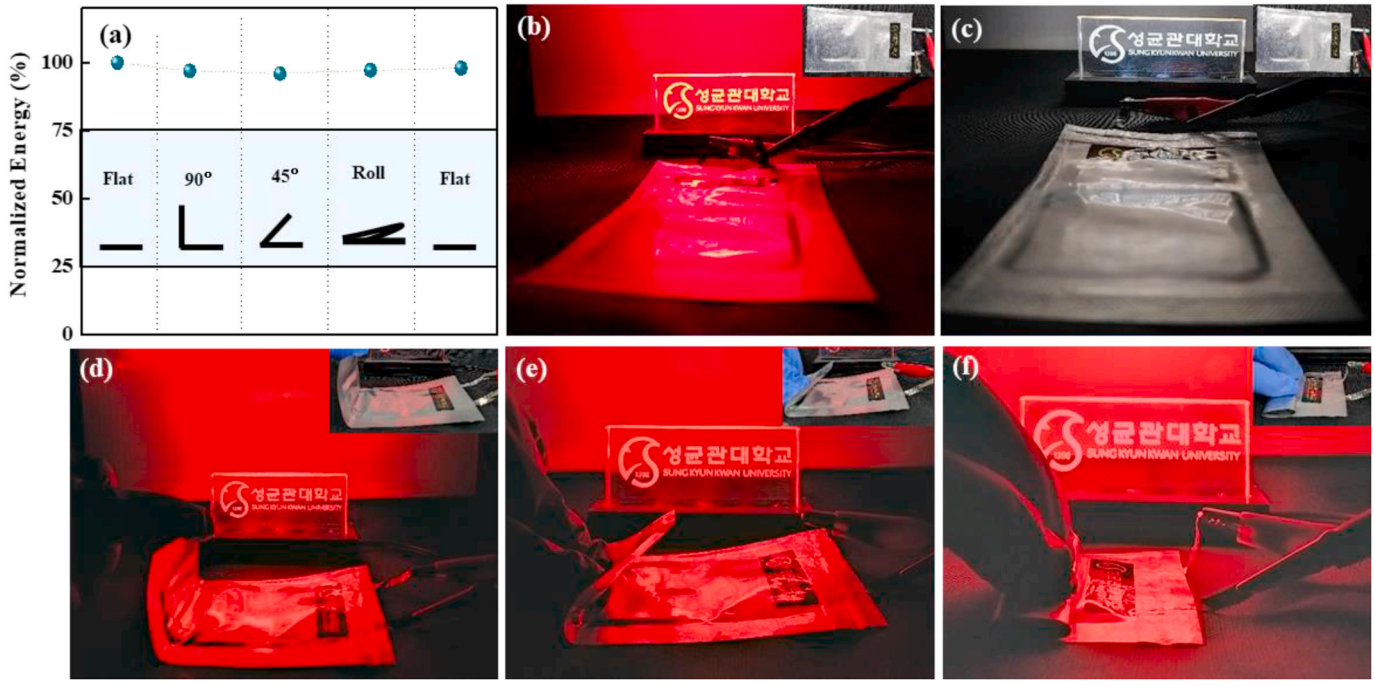

Fig. 6. (a) Normalized energy retention of flexible LICs under different folding conditions, and (b–f) digital photographs of flexible LIC powering LED lights under different bending conditions: (b) Flat – Red LED, (c) Flat – White LED, (d) 90° bend, (e) 45° bend, (f) roll. (For interpretation of the references to color in this figure legend, the reader is referred to the Web version of this article.)

the addition of 5.8 mL tetraethylorthosilicate in a dropwise under constant stirring for 24 h. Then washed with ethanol and dried throughout the night at 80 °C.

Synthesis procedure of SiO_2/NC nanosphere: The SiO_2/NC composite was synthesized by a thin film coating of nitrogen-doped carbon on the surface of SiO_2 nanosphere using guanine as a carbon and nitrogen source via a hydrothermal approach. One gram of guanine was dissolved in 75 mL of D. I water under continuous stirring for 30 min. Subsequently, 0.5 g of as prepared SiO_2 nanosphere was added into the above mixture. After this, the mixture was continuously stirred for 12 h. The resulting solution was transferred to 100 mL hydrothermal reactor flask and maintained at a temperature of 150 °C for 10 h. Then it was treated by filtration and washed with ethanol and distilled water for several times, and dried at 80 °C under vacuum for 12 h. Finally, the SiO_2/NC nanocomposite was obtained by carbonizing in a furnace at 800 °C 2 h under Argon atmosphere.

Material Characterization: Material phase formation and crystalline nature have been confirmed by X-ray diffractometer (Rigaku, Miniflex 600). The morphology of the samples was carried out using field-emission scanning electron microscopy (FE-SEM, Hitachi, S–4800II, 3 kV) and a thin osmium coating has given before analyzing the samples. In order to study the oxidation state and understand the bonding nature of the material, the sample was characterized by X-ray photoelectron spectroscopy using a JEOL JPS-900 in an ultra-high vacuum X-ray photoelectron spectrometer with an Al monochromatized cathode source at 25 W. Furthermore to understand the surface area and porous nature of the material by using Brunauer–Emmett–Teller (BET), Barrett–Joyner–Halenda (BJH) and Harkins–Jura (H–J) models with a Micromeritics Tristar ASAP 2020. Transmission electron microscopy (TEM) images were recorded by using a Philips TecnaiF20, Holland instrument at 200 kV acceleration voltage. Raman spectra were obtained by using a Lab Ram HR-800 (Horiba, Japan) Raman dispersive spectrometer with 514.5 nm laser excitation. Elemental analysis (C, N, and O) of the samples was performed by using a LECOCHN microanalyzer.

Fabrication of Li-ion Half Cells: The electrochemical performance of SiO_2 and SiO_2/NC was evaluated using CR2032 coin cells. The electrodes had the following composition: 80% active material, 10% Super P (conductive carbon), and 10% PVDF binder. The electrode slurry was rolled over Stainless foil, and then dried at 160 °C, 4 h in a vacuum oven. Lithium foil is used as the counter electrode, and polypropylene separators were employed. The electrolyte consisted of 1 M $LiPF_6$ in 1:1 (v/v) ethylene carbonate (EC): dimethyl carbonate (DMC).

Fabrication of Li-ion Hybrid Capacitor: LICs were also assembled in CR2032 coin cells utilizing SiO_2/NC as anode commercial activated carbon as cathode. Prior to LIC assembly, SiO_2/NC electrodes were pre-activated by directly contacting it with a lithium metal using electrolyte (1 M $LiPF_6$ in EC: DMC) for 5 h to achieve a major lithiation potential, a conventional process used for LIC fabrication. Commercial activated carbon (surface area: ~1880 $m^2\ g^{-1}$) was used as cathode. The cathode electrodes had the similar composition as anode, and were processed under similar conditions. The electrochemical performance of the commercial activated carbon was discussed in our previous work briefly. A fresh cathode was coupled with SiO_2/NC to realize a LIC device. For flexible LIC, the electrodes were sandwiched between P(VDF-HFP) membrane inside a polybag, and sealed inside a glovebox. Different bending/twisted tests were performed in the same flexible capacitor device. The fabrication process for P(VDF-HFP) membrane was given in our previous manuscript [38]. The P(VDF-HFP) membranes were soaked in 1 M $LiPF_6$ in EC: DMC electrolyte for 12 h to obtain the gel polymer electrolyte. Cyclic voltammetry and galvanostatic charge/discharge studies were performed using a Bio-Logic electrochemical workstation (SP-150, France) and a Won-A-Tech Battery tester (WBCS 3000, Korea), respectively. The power density of LIC was calculated as $P = (I\ V/2)\ W\ kg^{-1}$, where V is the working potential of LIC (V), and I is the current normalized by active mass in both electrodes ($A\ g^{-1}$), and the energy density of LIC was calculated as $E = (P \times t)\ Wh\ kg^{-1}$, where t is discharge time (h).

CRediT authorship contribution statement

Ranjith Thangavel: and, prepared the materials, and conducted the

electrochemical experiments, revised the manuscript written by. **Vignesh Ahilan:** prepared the materials, and conducted the electrochemical experiments, characterized the electrode materials, All the authors discussed and commented on the final manuscript. All authors have read and agreed to the published version of the manuscript.. **Megala Moorthy:** characterized the electrode materials, All the authors discussed and commented on the final manuscript. All authors have read and agreed to the published version of the manuscript.. **Won-Sub Yoon:** advised on electrochemical analysis, offered valuable comments on the work. **Sangaraju Shanmugam:** conceived the idea, offered valuable comments on the work. **Yun-Sung Lee:** and, offered valuable comments on the work.

Declaration of competing interest

The authors declare that they have no known competing financial interests or personal relationships that could have appeared to influence the work reported in this paper.

Acknowledgements

This work was supported by the National Research Foundation of Korea (NRF) grant funded by the Korea government (Ministry of Science, ICT & Future Planning) (No. 2019R1A4A2001527). Dr. Ranjith Thangavel acknowledges the support from National Research Foundation of Korea (NRF) grant funded by the Korea government (MSIT) (No. 2020R1C1C1014961). This work was also partly supported by the DGIST R&D Program of the Ministry of Science, ICT and Future Planning of Korea (20-ET-08).

Appendix A. Supplementary data

Supplementary data to this article can be found online at https://doi.org/10.1016/j.jpowsour.2020.229143.

References

[1] W. Lee, S. Muhammad, T. Kim, H. Kim, E. Lee, M. Jeong, S. Son, J.-H. Ryou, W.-S. Yoon, Adv. Energy Mater. 8 (2018), 1701788-1701788.
[2] S.-K. Jung, H. Kim, M.G. Cho, S.-P. Cho, B. Lee, H. Kim, Y.-U. Park, J. Hong, K.-Y. Park, G. Yoon, W.M. Seong, Y. Cho, M.H. Oh, H. Kim, H. Gwon, I. Hwang, T. Hyeon, W.-S. Yoon, K. Kang, Nature Energy 2 (2017), 16208-16208.
[3] B. Moorthy, S. Kwon, J.-H. Kim, P. Ragupathy, H.M. Lee, D.K. Kim, Nanoscale Horiz 4 (2019) 214–222.
[4] J.B. Goodenough, K.-S. Park, J. Appl. Comput. Sci. 135 (2013) 1167–1176.
[5] H. Wang, C. Zhu, D. Chao, Q. Yan, H.J. Fan, Adv. Mater. 29 (2017) 1702093.
[6] J. Ding, W. Hu, E. Paek, D. Mitlin, Chem. Rev. 118 (2018) 6457–6498.
[7] V. Aravindan, J. Gnanaraj, Y.-S. Lee, S. Madhavi, Chem. Rev. 114 (2014) 11619–11635.
[8] H. Jiang, P.S. Lee, C. Li, Energy Environ. Sci. 6 (2013) 41–53.
[9] C. Sun, X. Zhang, C. Li, K. Wang, X. Sun, Y. Ma, Energy Storage Mater 24 (2020) 160–166.
[10] R. Wang, Q. Zhao, W. Zheng, Z. Ren, X. Hu, J. Li, L. Lu, N. Hu, J. Molenda, X. Liu, C. Xu, J. Mater. Chem. 7 (2019) 19909–19921.
[11] J. Vetter, P. Novák, M. Wagner, C. Veit, K.-C. Möller, J. Besenhard, M. Winter, M. Wohlfahrt-Mehrens, C. Vogler, A. Hammouche, J. Power Sources 147 (2005) 269–281.
[12] H. Wang, C. Guan, X. Wang, H.J. Fan, Small 11 (2015) 1470–1477.
[13] V. Agubra, J. Fergus, Materials 6 (2013) 1310–1325.
[14] Z. Chen, I. Belharouak, Y.K. Sun, K. Amine, Adv. Funct. Mater. 23 (2013) 959–969.
[15] Y. Tang, L. Hong, Q. Wu, J. Li, G. Hou, H. Cao, L. Wu, G. Zheng, Electrochim. Acta 195 (2016) 27–33.
[16] D. Zhao, J. Qin, L. Zheng, M. Cao, Chem. Mater. 28 (2016) 4180–4190.
[17] B. Long, M.S. Balogun, L. Luo, Y. Luo, W. Qiu, S. Song, L. Zhang, Y. Tong, Small 13 (2017).
[18] L. Wan, J. Shen, Y. Zhang, X. Li, J. Alloys Compd. 708 (2017) 713–721.
[19] H. Yang, C. Zhang, Q. Meng, B. Cao, G. Tian, J. Power Sources 431 (2019) 114–124.
[20] E. Park, D.J. Chung, M.-S. Park, H. Kim, J. Power Sources 440 (2019) 227094.
[21] X. Zhao, X. Zhang, C. Li, X. Sun, J. Liu, K. Wang, Y. Ma, ACS Sustain. Chem. Eng. 7 (2019) 11275–11283.
[22] S. Zhang, C. Li, X. Zhang, X. Sun, K. Wang, Y. Ma, ACS Appl. Mater. Interfaces 9 (2017) 17136–17144.
[23] C.K. Chan, H. Peng, G. Liu, K. McIlwrath, X.F. Zhang, R.A. Huggins, Y. Cui, Nat. Nanotechnol. 3 (2008) 31–35.
[24] Y. Yao, M.T. McDowell, I. Ryu, H. Wu, N. Liu, L. Hu, W.D. Nix, Y. Cui, Nano Lett. 11 (2011) 2949–2954.
[25] N. Yan, F. Wang, H. Zhong, Y. Li, Y. Wang, L. Hu, Q. Chen, Sci. Rep. 3 (2013).
[26] T. Yang, X. Tian, X. Li, K. Wang, Z. Liu, Q. Guo, Y. Song, Chem. Eur J. 23 (2017) 2165–2170.
[27] L.-h. Yin, M.-b. Wu, Y.-p. Li, G.-l. Wu, Y.-k. Wang, Y. Wang, N. Carbon Mater. 32 (2017) 311–318.
[28] W.-S. Kim, J. Choi, S.-H. Hong, Nano Res 9 (2016) 2174–2181.
[29] W. Guo, X. Li, J. Xu, H.K. Liu, J. Ma, S.X. Dou, Electrochim. Acta 188 (2016) 414–420.
[30] J. Li, F. Zhang, C. Wang, C. Shao, B. Li, Y. Li, Q.-H. Wu, Y. Yang, Mater. Des. 133 (2017) 169–175.
[31] K. Zhu, Q. Wang, J.-H. Kim, A.A. Pesaran, A.J. Frank, J. Phys. Chem. C 116 (2012) 11895–11899.
[32] C. Han, J. Tong, X. Tang, D. Zhou, H. Duan, B. Li, G. Wang, ACS Appl. Mater. Interfaces 12 (2020) 10479–10489.
[33] Z. Chen, V. Augustyn, X. Jia, Q. Xiao, B. Dunn, Y. Lu, ACS Nano 6 (2012) 4319–4327.
[34] R. Thangavel, A.G. Kannan, R. Ponraj, G. Yoon, V. Aravindan, D.-W. Kim, K. Kang, W.-S. Yoon, Y.-S. Lee, Energy Storage Mater 25 (2020) 702–713.
[35] L.-F. Chen, S.-X. Ma, S. Lu, Y. Feng, J. Zhang, S. Xin, S.-H. Yu, Nano Res 10 (2017) 1–11.
[36] L. Fei, Q. Lin, B. Yuan, G. Chen, P. Xie, Y. Li, Y. Xu, S. Deng, S. Smirnov, H. Luo, ACS Appl. Mater. Interfaces 5 (2013) 5330–5335.
[37] M.-S. Park, H.-S. Woo, J.-M. Heo, J.-M. Kim, R. Thangavel, Y.-S. Lee, D.-W. Kim, ChemSusChem 12 (2019) 4645–4654.
[38] R. Thangavel, A.G. Kannan, R. Ponraj, M.-S. Park, H. Choi, D.-W. Kim, Y.-S. Lee, Adv. Mater. Interfaces 5 (2018) 1800472.
[39] R. Thangavel, R. Ponraj, A.G. Kannan, K. Kaliyappan, D.W. Kim, Z. Chen, Y.-S. Lee, Green Chem. 20 (2018) 4920–4931.
[40] S. Toyoda, J. Okabayashi, H. Kumigashira, M. Oshima, Appl. Phys. Lett. 83 (2003) 5449.
[41] Y. Li, H. Wang, L. Wang, Z. Mao, R. Wang, B. He, Y. Gong, X. Hu, Small 15 (2019) 1804539.
[42] R. Thangavel, A.G. Kannan, R. Ponraj, X. Sun, D.-W. Kim, Y.-S. Lee, J. Mater. Chem. 6 (2018) 9846–9853.
[43] Y.M. Kim, J. Jae, S. Myung, B.H. Sung, J.I. Dong, Y.K. Park, Bioresource tech 219 (2016) 371–377.
[44] J. Biemolt, I.M. Denekamp, T.K. Slot, G. Rothenberg, D. Eisenberg, ChemSusChem 10 (2017) 4018–4024.
[45] P.W. Xiao, L. Zhao, Z.Y. Sui, B.H. Han, Langmuir : the ACS journal of surfaces and colloids 33 (2017) 6038–6045.
[46] T. Yang, X. Tian, X. Li, K. Wang, Z. Liu, Q. Guo, Y. Song, Chemistry 23 (2017) 2165–2170.
[47] Z. Tan, K. Ni, G. Chen, W. Zeng, Z. Tao, M. Ikram, Q. Zhang, H. Wang, L. Sun, X. Zhu, X. Wu, H. Ji, R.S. Ruoff, Y. Zhu, Adv. Mater. 29 (2017).
[48] Q. Yu, J. Xu, C. Wu, J. Zhang, L. Guan, ACS Appl. Mater. Interfaces 8 (2016) 35264–35269.
[49] H.W. Park, D.U. Lee, M.G. Park, R. Ahmed, M.H. Seo, L.F. Nazar, Z. Chen, ChemSusChem 8 (2015) 1058–1065.
[50] Z. Zhang, J. Sun, M. Dou, J. Ji, F. Wang, ACS Appl. Mater. Interfaces 9 (2017) 16236–16242.
[51] Y. Mao, H. Duan, B. Xu, L. Zhang, Y. Hu, C. Zhao, Z. Wang, L. Chen, Y. Yang, Energy Environ. Sci. 5 (2012) 7950–7955.
[52] Y.Q. Li, J.C. Li, X.Y. Lang, Z. Wen, W.T. Zheng, Q. Jiang, Adv. Funct. Mater. 27 (2017).
[53] C. Tang, Y. Liu, C. Xu, J. Zhu, X. Wei, L. Zhou, L. He, W. Yang, L. Mai, Adv. Funct. Mater. (2017) 1704561.
[54] Z. Li, H. Zhao, P. Lv, Z. Zhang, Y. Zhang, Z. Du, Y. Teng, L. Zhao, Z. Zhu, Adv. Funct. Mater. (2018) 1605711.
[55] J. Ma, J. Sung, J. Hong, S. Chae, N. Kim, S.-H. Choi, G. Nam, Y. Son, S.Y. Kim, M. Ko, J. Cho, Nat. Commun. 10 (2019) 475.
[56] B. Moorthy, J.-H. Kim, H.-W. Lee, D.K. Kim, Energy Storage Mater 24 (2020) 602–609.
[57] M. Zhou, X. Li, B. Wang, Y. Zhang, J. Ning, Z. Xiao, X. Zhang, Y. Chang, L. Zhi, Nano Lett. 15 (2015) 6222–6228.
[58] E. Radvanyi, E. De Vito, W. Porcher, S.J.S. Larbi, J. Anal. At. Spectrom. 29 (2014) 1120–1131.
[59] Y. Zhang, Y. Li, Z. Wang, K. Zhao, Nano Lett. 14 (2014) 7161–7170.
[60] K. Song, S. Yoo, K. Kang, H. Heo, Y.-M. Kang, M.-H. Jo, J. Power Sources 229 (2013) 229–233.
[61] V. Aravindan, Y.S. Lee, S. Madhavi, Adv. Energy Mater. 5 (2015).
[62] T.S. Sahu, S. Mitra, Sci. Rep. 5 (2015) 12571.
[63] D. Shao, D. Tang, Y. Mai, L. Zhang, J. Mater. Chem. 1 (2013) 15068–15075.
[64] J.H. Won, H.M. Jeong, J.K. Kang, Adv. Energy Mater. 7 (2017) 1601355.
[65] G. Zhu, T. Chen, L. Wang, L. Ma, Y. Hu, R. Chen, Y. Wang, C. Wang, W. Yan, Z. Tie, J. Liu, Z. Jin, Energy Storage Mater 14 (2018) 246–252.
[66] H. Wang, Y. Zhang, H. Ang, Y. Zhang, H.T. Tan, Y. Zhang, Y. Guo, J.B. Franklin, X. L. Wu, M. Srinivasan, H.J. Fan, Q. Yan, Adv. Funct. Mater. 26 (2016) 3082–3093.
[67] H. Du, H. Yang, C. Huang, J. He, H. Liu, Y. Li, Nanomater. Energy 22 (2016) 615–622.
[68] H. Li, L. Peng, Y. Zhu, X. Zhang, G. Yu, Nano Lett. 16 (2016) 5938–5943.
[69] C. Zhao, Z. Li, H. Hu, Y. Yang, Y. Huang, J. Yang, J. Nanosci. Nanotechnol. 17 (2017) 729–734.
[70] F. Liu, J. Shen, W. Zhou, S. Zhang, L. Wan, RSC Adv. 7 (2017) 15992–15996.
[71] X. Liu, Y. Chen, H. Liu, Z.-Q. Liu, J. Mater. Sci. Technol. 33 (2017) 239–245.

[72] Y.-K. Kim, J.-W. Moon, J.-G. Lee, Y.-K. Baek, S.-H. Hong, J. Power Sources 272 (2014) 689–695.
[73] Y. Yao, J. Zhang, L. Xue, T. Huang, A. Yu, J. Power Sources 196 (2011) 10240–10243.
[74] J.-Y. Kim, D.T. Nguyen, J.-S. Kang, S.-W. Song, J. Alloys Compd. 633 (2015) 92–96.
[75] J. Meng, Y. Cao, Y. Suo, Y. Liu, J. Zhang, X. Zheng, Electrochim. Acta 176 (2015) 1001–1009.